4.4 Model Systems in Catalysis for Energy Economy

Niklas Nilius, Martin Sterrer, Shamil Shaikhutdinov,
Dietrich Menzel, and Hans-Joachim Freund

4.4.1 Introduction

Harvesting, saving, and storing energy are key issues in today's general energy discussions [1]. Harvesting energy through photochemistry and storing energy in compounds using thermal energy-efficient processes are attractive solutions to some problems within the grand picture [2].

Heterogeneous thermal and photocatalysis are bound to play a key role in those solutions. However, while thermal heterogeneous catalysis is widespread in chemical industries, and photocatalysis not yet, there is still a strong demand in both areas for research in order to understand the process and its elementary steps as well as to rationally design the catalytic material.

Investigation of model catalysts can play a decisive role in a rational approach to understand heterogeneous catalysis, and this is the topic of this chapter [3–6].

In the introduction, the model systems will be defined to familiarize the reader with the approach in order to appreciate the connection to real-world catalysis. Following the introduction, we will demonstrate via four case studies various fundamental aspects in thermal and photocatalysis whereby studies on model systems might become important to unravel the foundations of reaction mechanisms.

The model systems have been created under the premises that it is possible to investigate them at the atomic scale using the toolbox that has been developed in surface science during the second half of the last century up to now [7].

The model systems are based on the idea to grow well-ordered oxide layers or thin films, representing the bulk material, and as such the catalyst support, on single-crystal metal surfaces using the concepts of epitaxial growth [8]. This, in turn, allows one to investigate bulk insulators without having to worry about charging when charged information carriers such as electrons or ions are used to investigate those systems. One thus avoids one of the key difficulties hampering the detailed study of real catalysts. Also the application of scanning probe techniques including electron tunneling is possible for thin-film systems. The fact that the oxides are grown on a metal support also ensures the easy applicability of infrared reflection absorption spectroscopy at such systems. Moreover, controlling the growth parameters of the oxide film also allows one to vary the density of defects at the surface of the oxide films, a factor of importance when nanoparticles are grown on the oxide support.

The first case study presented in this paper is related to a model system that is schematically represented in Figure 4.4.1A [9]. An oxide film representing the bulk material is grown on a metal surface. The growth of metal nanoparticles (MNPs), and in particular their morphologies, which may distinctively influence the catalytic performance, are compared on pristine oxide films and films that have been doped with metal ions that may assume higher valences than the metal of the host material. Using the model system, even the effect of doping as a function of the depth (Figure 4.4.1A) at which the dopant is deposited below the surface may be studied, and thus questions of the presence of dopants in materials used to prepare supports in real catalysis may be addressed.

Real dispersed metal catalysts are prepared by precipitation from solution. Investigating processes involving oxide surfaces in solution is a challenging topic. Figure 4.4.1B schematically shows the type of system investigated [10]. Particles are deposited from an aqueous solution of a metal chloride as a function the pH
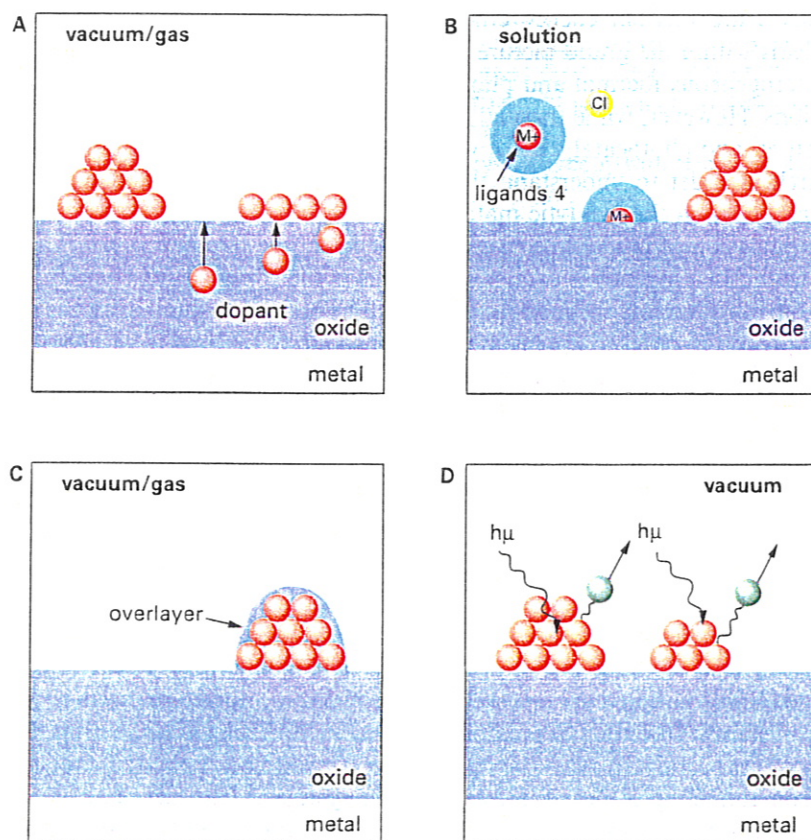

Figure 4.4.1 Schematic representation of the model systems discussed within the chapter: (A) nanoparticle growth influenced by dopants in the support, (B) nanoparticle deposition from solution, (C) strong metal support interaction, and (D) photochemistry at supported nanoparticles as a function of size.

of the solution. The pH strongly influences the outcome of the impregnation process. Understanding the details of such processes is of utmost importance for preparation of technical catalysts, and the first steps in this direction are being taken. This represents the second case study.

In a third case study, the effect of a reducible support material, such as magnetite, on Pt nanoparticles anchored onto the magnetite surface after a heat treatment is investigated. In this system, a typical strong metal–support interaction (SMSI) – that is, the migration of a thin oxide film from the support onto the metal nanoparticles influencing catalytic performance – has been observed. An SMSI effect usually renders the system inactive in oxidation reactions such as CO oxidation. Here it is shown that depending on the chemical potential of oxygen in the gas phase, the SMSI system schematically shown in Figure 4.4.1C may become more active than the clean metal at the given temperature. Some general design principles may be deduced from those studies [11, 12].

In the fourth and last case study, the interaction of laser light with alumina-supported silver nanoparticles (Ag NPs) and the consequences for the desorption of molecules were studied. In particular, the question of tuning the light frequency into the plasmon frequency of the particles and thus optimizing the harvesting of energy has been investigated as a function of particle size. Also, the consequences of varying the duration of the laser pulse from nanoseconds to femtoseconds, addressing more fundamental questions, are discussed. This is schematically indicated in Figure 4.4.1D [13–15].

This chapter does not provide the space to discuss all aspects of model catalyst studies in detail, but the four case studies exemplify the breadth and depth that is provided by such investigations.

4.4.2 First Case Study: Controlling Nanoparticle Shapes on Nondoped and Doped Oxide Supports

The performance of metal-particle ensembles in catalytic reactions is not only governed by the size and shape of the deposits but also by their interactions with the oxide support. The occurrence of certain active sites on a catalyst surface is often related to distinct particle geometries. For example, perimeter sites that enable a molecule to interact simultaneously with the metal and the oxide surface are most abundant on flat metal islands, while low-coordinated metal atoms are usually found on ultrasmall aggregates [16–18]. Moreover, the geometry affects the electronic properties of metal particles, and many phenomena such as metal-to-insulator transitions are closely related to the atom arrangement within the aggregate [19]. Also, in photocatalysis, particle shapes are of utmost importance as they determine the energy position of plasmonic excitations, being the initial step in several photon-mediated processes [20]. The dependence of the chemical reactivity of a supported metal catalyst on size and morphology of the active metal species has been explored in detail for gold [21]. Using transmission electron microscopy, raft-shaped Au islands on Fe_2O_3 support have been identified as the active species for the low-temperature

CO oxidation [22, 23]. A similar conclusion was drawn from scanning tunneling microscopy (STM) measurements on the Au/TiO$_2$ system, where again bilayer high deposits turned out to be the most active ones [24, 25]. Naturally, a close structure-reactivity relationship is not restricted to Au particles but can be found for other metal species in a multitude of chemical reactions [26].

Given the importance of the particle geometry, a good fraction of catalysis research has been devoted to exploring different means to optimize this parameter. In principle, particle morphologies are governed by the strength of the metal-support interaction with respect to the surface-free energies of the separated systems. For oxide supports, as commonly used in heterogeneous catalysis, this usually leads to the formation of three-dimensional (3-D) deposits, as both the free energy of the oxide surface and the interface adhesion of the ad-metal are small (Figure 4.4.2A). Moreover, the metal particles tend to mimic the symmetry of the oxide lattice in order to establish interfacial bonds. This causes, for instance, the Ni lattice to switch from face centered cubic (fcc) in the bulk to hexagonal close packed (hcp) in small deposits grown on the MgO(001) surface [27]. To overcome these growth restrictions, several procedures have been developed that enable a certain control of particle equilibrium shapes on oxide supports. Most of them are based on a targeted modification of the substrate morphology, for example, by introducing defects [28] and suitable ad-species (i.e. hydroxyl groups) [29]. Their function is to anchor the metal particles on the inert oxide surface, inhibiting sintering and ripening processes (Figure 4.4.2A). Alternatively, oxide surfaces with polar character might be used because they feature high surface-free energies and therefore an enhanced adhesion of the ad-metal [30, 31]. This approach has been demonstrated for the polar ZnO(0001) surface, where Cu was found to grow in a layer-by-layer fashion [32]. Finally, electron transfer processes across the metal-oxide interface can be exploited to alter the equilibrium shape of the ad-particles [33]. The charge exchange between metal deposits and support is stimulated by different mechanisms. On thin oxide films grown on metal substrates, it often occurs spontaneously due to the different Fermi levels in support and ad-metal. The accumulation of excess charges in the deposit thereby activates new charge-mediated coupling schemes between both systems, such as polaronic and Coulomb-type interactions. The enhanced interface adhesion promotes a spreading of the metal on the oxide support and might, in an extreme case, switch the growth regime from 3-D to two-dimensional (2-D) when going from neutral to charged ad-species [34, 35]. The charge transfer is, however, restricted to ultrathin oxide films, as it requires electron tunneling through the insulating layer.

A charge-induced formation of low-dimensional metal aggregates has been identified on various oxide thin films, employing mostly STM as the imaging tool. On alumina films grown on NiAl(110), for example, the formation of one-dimensional (1-D) gold chains was observed (Figure 4.4.2C) [36]. The linear nature of the aggregates enables good spatial separation of the extra electrons inside the particle electronic system, which in turn lowers the internal Coulomb repulsion. With increasing atom number, the equilibrium shape changes to planar 2-D islands, as observed for gold on magnesia thin films [34]. By analyzing the electronic structure of the 2-D islands, their charge state could be quantified directly [37]. For a planar Au$_{18}$ aggregate on 2 monolayer (ML) MgO/Ag(001) for example, four extra electrons were
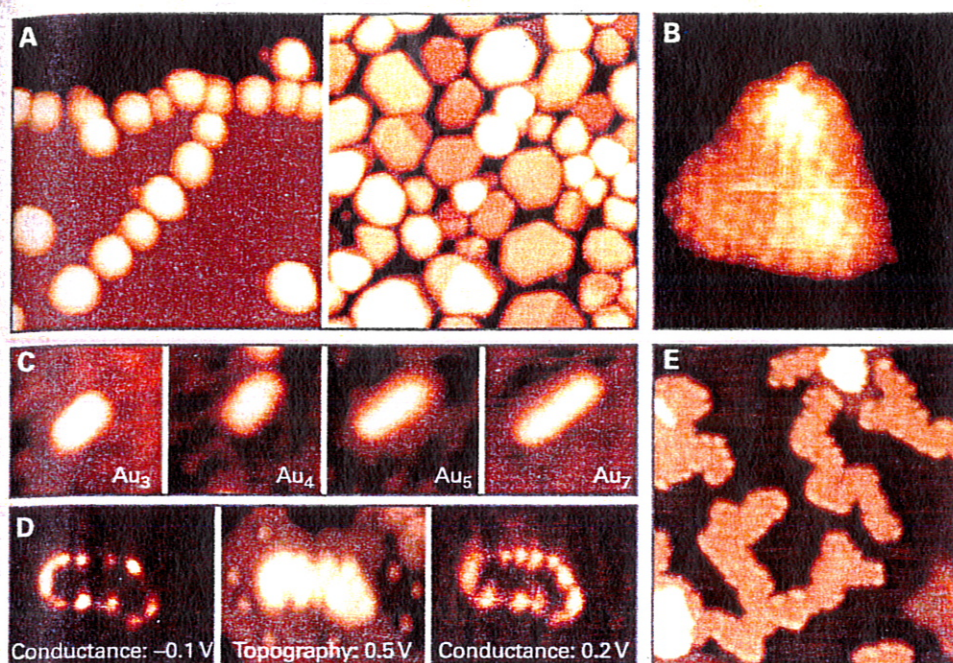
Figure 4.4.2 (A) STM images of Ag particles on pristine and sputtered Al_2O_3 films grown on NiAl(110) (1 V, 100 × 100 nm^2). Note the different particle density and shape on the defect-rich oxide surface. (B) Atomically resolved image of the top facet of a Pd particle on Al_2O_3/NiAl(110) (0.05 V, 4 × 4 nm^2). The facet is well ordered and corresponds to a Pd(111) plane. (C) One-dimensional Au clusters on ultrathin alumina films that develop as a result of a charge transfer out of the support (−1.0 V, 5 × 5 nm^2). (D) Two-dimensional Au island on a 2 monolayer (ML) MgO/Ag(001) film. Whereas the central panel displays the island morphology (0.2 V, 25 × 25 nm^2), the left and right panels are conductance images and reflect the state density at the given bias voltage. (E) Large monolayer high Au sheets on MgO thin films with characteristic meandering shapes (0.2 V, 25 × 25 nm^2).

found to reside on the deposit, providing a rough idea of the efficiency of charge transfer processes across the metal-oxide interface. The relationship between the preferred growth geometry in the presence of excess charges and the need of the system to minimize the internal electron-electron repulsion has been visualized best for even larger Au islands on the MgO support [38]. The transferred charges from the support localize exclusively at the perimeter of the metal island, where electron-rich edge states with Au 6s character become visible in tunneling spectroscopy (Figure 4.4.2D). As the electron-storage capacity of those edge states is limited, the gold islands develop a peculiar meandering shape that keeps the ratio between inner and edge atoms constant (Figure 4.4.2E). The electron-rich nature of their perimeter renders charged monolayer Au islands particularly attractive for adsorbates. Not surprisingly, CO molecules dosed onto the Au/MgO thin-film system were found to bind exclusively to the low-coordinated edge atoms, while no adsorption takes place in the island interior [39]. According to density functional theory

(DFT) calculations, the island perimeter is also prone to bind and dissociate O_2 molecules, being the initial step to form gold oxide at the island perimeter [40].

Although charge-mediated growth schemes are ideally suited to alter the equilibrium shape of metal particles on thin oxide films, the mechanism breaks down on thick, bulk-like oxide supports as used in real catalysts. The reason is the limited tunneling length of electrons through an insulating oxide, being on the order of 1–2 nm. An obvious approach to overcome this restriction is to insert the charge donors directly into the oxide material, preferentially into a near-surface region. By this means, charge transfer into the ad-metal can be sustained even for arbitrarily thick oxide slabs, preserving the previously discussed possibility to tailor the particle shapes. There are two types of donor-like impurities in an oxide material. The first one comprises intrinsic lattice defects that are able to trap and release electrons [41]. Prominent examples are single O vacancies that contain one or two excess electrons (F^0 or F^+ centers) and structural lattice defect with electron-trapping abilities. For example, grain boundaries that are present in most oxide films were found to trap large quantities of extra electrons (up to 5 per nm defect line) [42, 43]. The subsequent transfer of electrons out of these defects into suitable metal deposits has been demonstrated for the Au/MgO_{1-x} system, employing infrared absorption spectroscopy with CO as probe molecule [39, 44]. The main disadvantage of using intrinsic lattice defects as electron donors is the strong variation of their concentration with the oxide preparation conditions. Whereas the abundance of oxygen vacancies depends on the O_2 chemical potential during preparation or reaction conditions, the density of structural defects is given by the mechanical strain exerted on the oxide lattice during growth. Both influences cannot easily be controlled in real materials used for catalysis and energy storage and are hence unsuitable to tailor the equilibrium geometry of ad-particles.

The second approach exploits new charge degrees of freedom that can be inserted into an oxide lattice by replacing some of the intrinsic ions with foreign species [45–50]. Whereas doping has proved to be extremely successful for tailoring the properties of semiconductors, a transfer of this technique to oxides is challenging due to the higher complexity of the latter material. Two general approaches can be distinguished, which include overvalent doping (i.e. replacing a lattice ion with a species of higher charge state) and undervalent doping where an electron-poor ion substitutes the original species. While the dopants have donor character in the first case (i.e. they release electrons to suitable adsorbates), they act as electron acceptors in the latter by creating hole states in the oxide that stimulate electron transfer out of the adsorbates. In both scenarios, the localization of excess charges in the ad-metal might lead to distinct changes of its geometric and electronic properties, in a similar fashion as described for thin oxide films before.

The impact of doping on the growth geometry of metal particles has been demonstrated for CaO films doped with Mo impurities in the 1%–2% range [9]. After dosing gold onto the atomically flat CaO(001) surface, a perfectly 2-D growth regime was detected with the metal spreading into large monolayer high islands on the oxide support (Figure 4.4.3). This unusual growth behavior is not observed on nondoped films, where tall 3-D Au deposits develop as expected from the weak interaction between the wide-gap insulator and the ad-metal. The observed crossover in growth
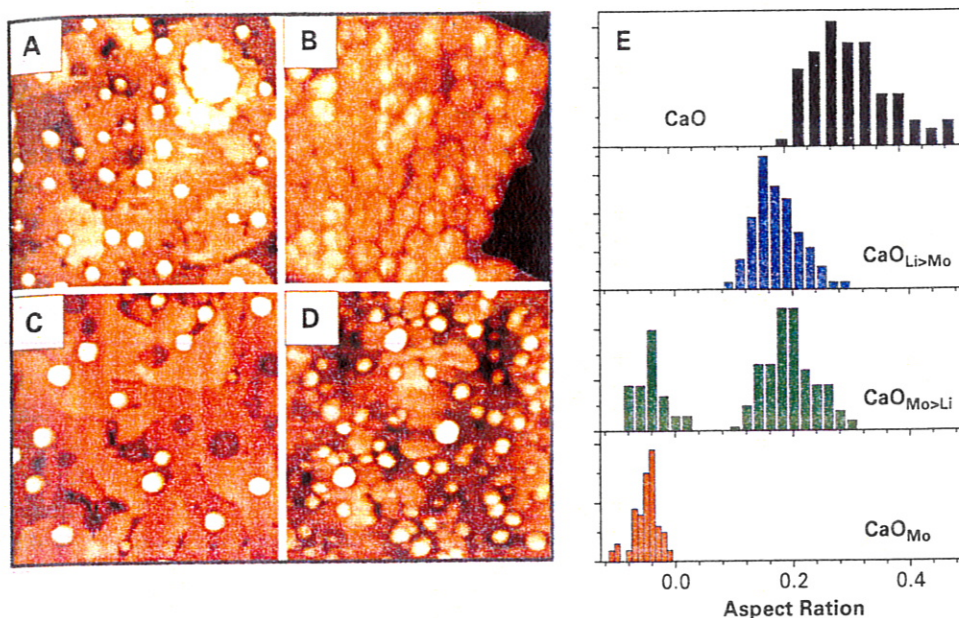
Figure 4.4.3 STM images of 0.5 monolayer (ML) Au deposited onto (A) pristine CaO, (B) CaO doped with 4% Mo, (C) CaO doped with 4% Mo plus 2% Li, and (D) CaO doped with 4% Mo plus 8% Li (6.0 V, 50 × 50 nm²). Whereas the presence of Mo donors changes the Au morphology to 2-D, codoping with Li reinstalls the original 3-D growth mode. Note that monolayer Au islands in (C) appear as depressions, as their conductance is lower than the one of bare CaO(001). (E) Histogram of aspect ratios for Au particles grown on the differently doped CaO films. The low aspect ratios observed for Mo-rich samples correspond to a wetting growth of gold, as induced by electron transfer from the donor-type impurities.

morphology is in full agreement with the donor character of the Mo impurities. Without gold, the Mo ions adopt a 2+ charge state that is typical for cations in the rock-salt lattice. This implies that the Mo $3d$ electrons remain localized in the dopant, occupying t_{2g}-type defect states inside the CaO band gap [9]. However, some of the d-electrons are close to the onset of the CaO conduction band and hence in an energetically unfavorable situation, which renders a transfer into suitable acceptor states likely. Exactly those states are now provided by the Au ad-atoms, and indeed a spontaneous electron crossover takes place from a high-lying Mo d-state into the Au $6s$ affinity level. The anionic gold exhibits a reinforced bonding to the CaO surface, stimulating the 2-D growth regime revealed in the experiment (Figure 4.4.3A, B).

The interrelation between electron transfer and realized Au particle shape can be proved directly by blocking the electron flow between the dopants and the ad-metal, for example, by introducing a defined number of electron traps into the oxide lattice. As discussed before, hole states with electron-trapping abilities are generated by undervalent dopants (e.g. by monovalent Li⁺ ions sitting in Ca²⁺ substitutional sites). Indeed, a codoping of CaO with both Mo and Li leads to an internal charge

compensation of the two dopants, in which the excess electrons of the donors are trapped by the hole states inserted by the acceptor species [51]. As a consequence, no electron transfer into the Au ad-metal takes place anymore for the codoped CaO films, and the Au deposits adopt the original 3-D equilibrium shape that is typical for pristine CaO (Figure 4.4.3C, D). Apparently, the desired doping effect gets cancelled out if dopants with opposite charge state coexist in the oxide host.

Interestingly, not every overvalent dopant is able to donate charges into an ad-metal. Cr ions embedded in an MgO matrix, for instance, are inappropriate electron donors, and the Au growth morphology is hardly affected in this case [52]. The reason is that Cr in the MgO lattice cannot be stabilized in the 2+ charge state because it prefers a high-spin configuration and consequently puts electrons into both the low-lying t_{2g} and the high-lying e_g state manifold. The latter already overlaps with the MgO conduction band, so that the electrons move away from the dopant and become trapped in other oxide defects, preferentially in Mg vacancies sites [53]. The Cr adopts a 3+ charge state right from the beginning and cannot donate further charges to surface species. An active dopant therefore needs to fulfill two requirements. On the one hand, it should occur in two stable charge configurations in the oxide host. On the other, the top-most occupied state needs to be high enough in energy to render charge transfer into an adsorbate affinity level energetically feasible. The same considerations also hold for acceptor-like dopants, only that the hole state produced upon doping localizes in an adjacent oxygen ion. It should be noted that holes in the oxygen $2p$ states are intrinsically unstable against charge transfer from competing electron sources, such as electron-rich O defects (F^0 centers) or donor-type molecules that are always present on oxide surfaces (water, hydrogen) [54, 55]. Hole doping as a means to tailor the properties of metal ad-particles is hence more difficult to realize than electron doping with donor-type impurities.

In conclusion, the doping of oxide materials opens promising new routes to change the morphology and electronic properties of supported metal particles as used in heterogeneous catalysis. Thin oxide films are ideally suited to elucidate such doping effects, as they can be explored by means of conventional surface science techniques at a fundamental level. The identified mechanisms can be transferred to real catalysts later, as the doping approach is not based on specific thin-film effects.

4.4.3 Second Case Study: Preparation of Oxide-Supported Palladium Model Catalysts by Pd Deposition from Solution

In typical surface science experiments as presented previously, oxide-supported metal nanoparticles are deposited onto a clean oxide surface by physical vapor deposition. The precursor in this process is metal atoms in the gas phase, which impinge on the surface, diffuse until they eventually get trapped (either at surface defects or by dimer formation), and then act as nuclei for the growth of larger particles. These processes are well understood for ideal model systems under ultrahigh vacuum (UHV) conditions [56, 57]. In contrast, most "realistic" supported metal catalyst

preparation procedures (e.g. impregnation) make use of metal complexes as the precursor, primarily in the form of salts dissolved in aqueous solution, which adsorb at the support-solution interface in the initial step [58, 59]. The pH of the solution is one of the important parameters, as it controls the interaction of precursor complexes with the support by determining the speciation of the solution complexes as well as the surface charge of the support. Based on the knowledge of the pH-dependent precursor speciation in solution on one hand, and the properties of the support (point of zero charge, PZC, density of hydroxyl groups) on the other, this interaction can be described phenomenologically by complexation models [60]. The transformation of the adsorbed precursor complex into the catalytically active compound then usually involves a calcination step followed by reduction. The performance in a catalytic test reaction is the ultimate criterion for the usefulness of a certain preparation procedure. While prereaction, in situ, and postreaction characterization of the catalyst provides relevant information about the active sites in the catalytic reaction, initial nucleation and decomposition of the adsorbed precursor into metal nanoparticles are difficult to track experimentally with powder catalysts and remain largely unknown aspects of catalyst preparation. As will be shown in the following, single-crystalline oxide thin films are ideally suited for studying these processes, provided they are stable at typical impregnation conditions.

We have chosen to use $Fe_3O_4(111)$ films grown on $Pt(111)$ for studying the deposition of palladium from a $PdCl_2$ precursor. $Fe_3O_4(111)$ films with a thickness of ~10 nm were prepared in a UHV chamber following a recipe described in the literature [61]. The surface of the films was subsequently covered by precursor solution, which was prepared from an acidic (5 M HCl) $PdCl_2$ stock solution by dilution to the desired concentration and pH adjustment with NaOH. Following washing with water and drying under a stream of He, the sample was then subjected to thermal treatment in UHV to transform the adsorbed Pd precursor into nanoparticles.

Shown in Figure 4.4.4 are STM images (taken in air) of $Fe_3O_4(111)$-supported Pd particles formed by impregnation with 5 mM Pd precursor solutions of different pH ranging from 1.3 to 10 and after a final thermal treatment at 600 K in UHV. In the acidic pH range (pH 1.3 to pH 4.7), we observe a substantial variation of Pd coverage, particle size, and particle dispersion. At the lowest pH, only a few Pd particles with a diameter of 1 nm are present (note that after impregnation, the surface of the $Fe_3O_4[111]$ film is affected by heating leading to the observation of meandering features, most prominently seen for pH 1.3; on top of this surface, the Pd particles appear as small spots). As the pH of the impregnation solution is changed to 1.6 and 2.5, higher Pd coverage is obtained with a slight increase of particle diameter, however, with still uniform size distribution. The behavior in this pH range reflects the results of typical uptake curves [62] for negatively charged precursor complexes (here $PdCl_4^{2-}$) on positively charged support surfaces ($PZC[Fe_3O_4] \approx 8$). The retardation of Pd uptake in strongly acidic medium may be ascribed to (i) competitive adsorption of chloride [63] or (ii) a decrease of the adsorption equilibrium constant at high ionic strength [64]. As the pH is increased to 4.7, the very unfavorable situation of uncontrolled deposition of large and nonuniformly sized Pd particles occurs. Such deposition characteristic has been observed with various near-neutral pH precursor solutions and can be explained by deposition of solution-precipitated
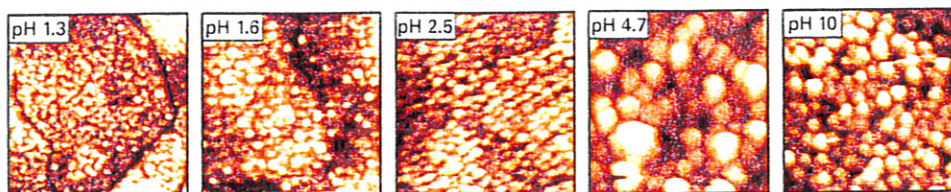
Figure 4.4.4 STM images (100×100 nm^2) of Pd particles formed on Fe$_3$O$_4$(111)/Pt(111) thin films by impregnation with Pd precursor solution of different pH prepared from PdCl$_{2,aq}$ and subsequent annealing in UHV to 600 K.

Pd particles. At alkaline pH (pH 10, Figure 4.4.1) the Pd particle size distribution in the final catalyst is again uniform. However, compared to the acidic pH range, a significantly higher Pd loading is achieved.

A more detailed account on the nucleation process of Pd nanoparticles from adsorbed precursor complexes is given in Fig. 4.4.5, which compares STM and X-ray photoelectron spectroscopy (XPS) results obtained at different annealing temperatures after impregnation of Fe$_3$O$_4$(111)/Pt(111) with precursor solutions of pH 1.3 (15 mM Pd^{2+}) and pH 10 (2 mM Pd^{2+}), respectively. The combination of STM and XPS allows the thermal evolution of morphological features with the chemical nature of the precursor species to be directly correlated. In the case of acidic precursor solution (Figure 4.4.5A, [10]), the STM image obtained directly after removing the precursor solution without additional heating (room temperature, RT) shows a low density of particles on a seemingly clean Fe$_3$O$_4$ substrate. As the temperature is increased to 390 K, the particle density is increased, and at a final temperature of 600 K, particles uniformly cover the Fe$_3$O$_4$ surface (Figure 4.4.5A). Note that the particle size (2 nm) does not change from RT to 600 K, showing that 600 K is well below the onset of Ostwald ripening under the present experimental conditions. The corresponding Pd 3d XPS spectra (Figure 4.4.5B) reveal the presence of two Pd species with binding energies (BEs) of 337.8 and 336.2 eV (Pd 3$d_{5/2}$) on the Fe$_3$O$_4$ sample directly after removing the pH 1 solution. With increasing temperature, the Pd component at higher BE is gradually transformed into the lower BE component. This behavior is perfectly in line with the STM observations and allows the high BE component to be assigned to adsorbed Pd precursor complexes, which cannot be resolved with STM. The low BE component, on the other hand, correlates with the emergence of nucleated particles at increasing annealing temperature. The chemical identity of the surface species may be inferred from knowledge of the solution speciation of Pd. It is safe to assume that in pH 1.3 (HCl) solution, Pd is present as PdCl$_4^{2-}$ complex. The high Pd 3$d_{5/2}$ BE obtained for the adsorbed species at RT (337.8 eV, compared to 335.2 eV for bulk Pd) is in line with previous observations [65, 66] and can, therefore, be attributed to adsorbed PdCl$_4^{2-}$ or aquochloro complexes of the form Pd(H$_2$O)$_x$Cl$_y^{n-}$. According to STM results shown in Figure 4.4.5A, these adsorbed precursor complexes are thermally decomposed into Pd particles. At a final annealing temperature of 600 K, the BE of the particles is 335.7 eV, which is significantly higher than expected for metallic Pd particles. XPS analysis
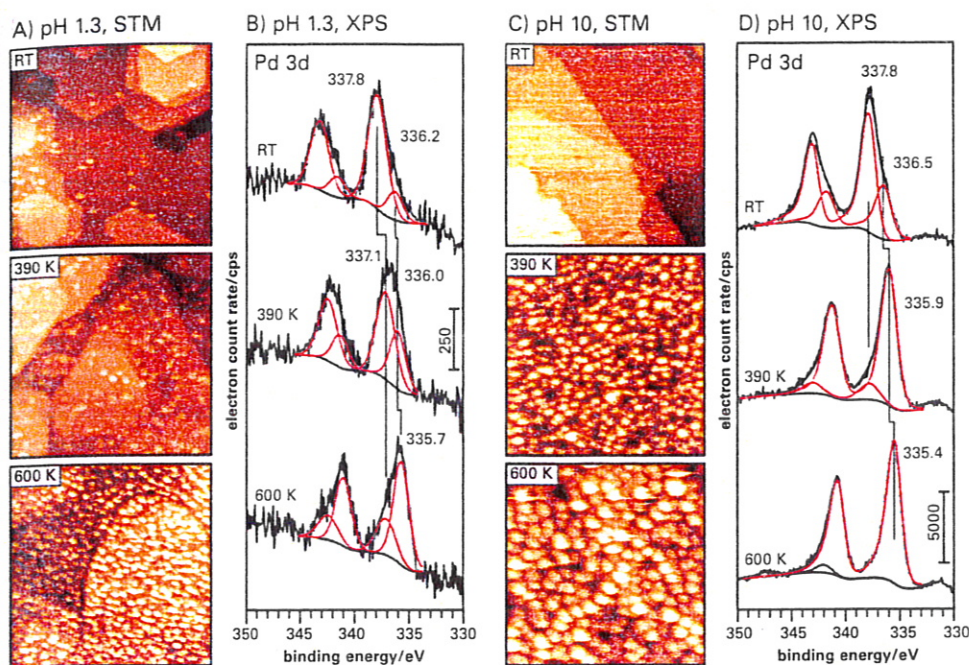
Figure 4.4.5 STM and XPS results for Pd deposited on Fe$_3$O$_4$(111)/Pt(111) surfaces from (A and B) pH 1 precursor solution and (C and D) pH 10 precursor solution at different stages of pretreatment: directly after removing the precursor solution at room temperature (top), after drying in UHV at 390 K (middle), and at 600 K (bottom).

suggests that this BE shift results from remaining chlorine adsorbed on the Pd particles rather than from a particle size effect [10].

A slightly different behavior is observed on the Fe$_3$O$_4$ sample contacted with pH 10 precursor solution (Figure 4.4.5C and 4.4.5D, [67]). In the initial state, no particles are observed, suggesting that the surface is uniformly covered by adsorbed precursor. Only moderate drying at 390 K leads to the formation of small particles in the size range 1–2 nm covering the entire surface. The corresponding XPS spectrum shows the dominant abundance of a single Pd species with a Pd $3d_{5/2}$ BE of 335.9 eV. Significant particle sintering (average diameter 4–5 nm) occurs upon further annealing with a concomitant shift of the Pd $3d_{5/2}$ component to 335.4 eV. The different nucleation behavior observed on the pH 10 sample as compared to the pH 1.3 case is a result of the different speciation of Pd complexes. At pH 10, the adsorbed Pd species are hydroxo complexes. Their thermal decomposition into Pd nanoparticles proceeds via the formation of PdO particles as an intermediate step (observed at 390 K).

Based on the results presented in Figure 4.4.4 and Figure 4.4.5, the deposition of Pd on single-crystalline Fe$_3$O$_4$(111) thin films from aqueous precursor solutions can be divided into three different regimes: electrostatic adsorption of PdCl$_4^{2-}$, precipitation, and adsorption of Pd hydroxide. In the acidic pH range (< pH 3), the interaction is controlled by electrostatic adsorption of the negatively charged precursor

complex ($PdCl_4^{2-}$) and the positively charged surface. If we apply this so called "strong electrostatic adsorption" concept to the present case we expect the following behavior: A minimum uptake at the PZC of the oxide is predicted, followed by a maximum below the PZC, and, again, a small uptake at small, i.e. acidic, pH [60]. The latter case, which is usually ascribed to the effect of high ionic strength, has been observed here. In this regime, small and uniformly sized Pd particles are formed by thermal decomposition of the adsorbed precursor. The regime of maximum adsorption due to strong electrostatic interaction could not be reached because uncontrolled deposition of precipitated Pd (most probably $PdCl_2$) species sets in at near-neutral pH. Shifting the solution pH into the basic range (pH 10) leads again to the formation of Pd particles with uniform size distribution after decomposition of the precursor. Strong electrostatic adsorption is not possible in this regime because both the solution complexes ($Pd[OH]_4^{2-}$) and the oxide surface are negatively charged. A chemical interaction between precursor and support (e.g. hydrolytic adsorption of Pd hydroxide) is more likely the dominant interaction at the support-solution interface at basic pH.

In summary, the way is paved to look at oxide-supported metal nanoparticles, prepared in solution, and to understand the formation of MNPs through calcination and reduction. However, there is still a way to go to identify the elementary steps in the interaction of the species from solution at the solid-liquid interface. Of course, this is what we really want.

4.4.4 Third Case Study: Strong Metal/Support Interaction Effects

SMSI effects have been known for many years to occur when a metal catalyst supported on a reducible oxide is subjected to high-temperature treatments in a reducing atmosphere (typically, hydrogen) [68–72]. In principle, the SMSI state depends on the metal, the oxide, and the reaction and may include both structural and electronic effects. The most prominent example is Pt supported on TiO_2, which undergoes SMSI via the formation of a thin titania film overgrowing the Pt particles, albeit of a very complex structure [73–75]. Certainly, the oxide overlayer suppresses adsorption of many molecules otherwise readily adsorbing on a metal surface and, as a result, renders metal catalysts inactive. However, when the encapsulated oxide film is very thin ("ultrathin"), the situation is not straightforward since structural and chemical properties of an ultrathin film are often considerably different from those of a bulk counterpart [76]. In some cases, the encapsulation may lead to the promotional effects. Here, we illustrate this phenomenon for Pt particles supported on iron oxide $Fe_3O_4(111)$.

The Pt particles were formed by physical vapor deposition onto ~10 nm thick $Fe_3O_4(111)$ films grown on Pt(111). The particles become more uniform in size and well-faceted upon heating to elevated temperatures. Figure 4.4.6 shows typical morphology of the Pt nanoparticles vacuum-annealed at temperatures above 800 K. The particles, about 1 nm in height and 5 nm in width, expose atomically
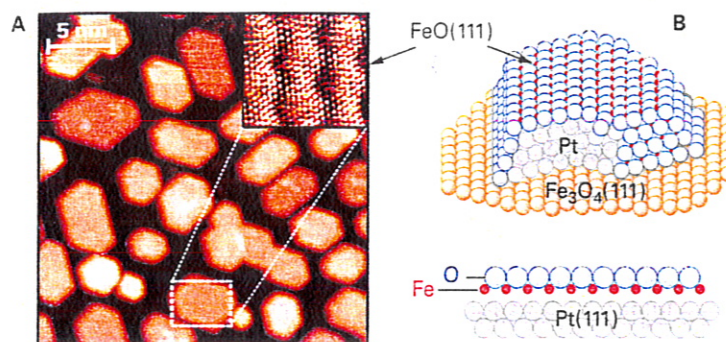
Figure 4.4.6 (A) Typical STM image of Pt deposited onto $Fe_3O_4(111)$ film and subsequently annealed in UHV at 850 K. Atomically resolved STM image of the top facet is shown in the inset. (B) The cross view of the FeO(111)/Pt(111) interface and schematic presentation of the Pt particles encapsulated by the FeO(111) overlayer.

flat top facets, which are Pt(111) in nature, owing to the epitaxial relationships between $Fe_3O_4(111)$ and Pt(111) [77]. It has turned out, however, that high-temperature annealing leads to a dramatic attenuation of the CO uptake compared to the samples annealed at 600 K, which cannot be assigned solely to Pt sintering [77, 78]. This behavior is, in fact, a "classical" manifestation of the SMSI [68].

High-resolution STM study showed that the top facets exhibit the hexagonal lattice of protrusions with a ~3 Å periodicity, in turn forming a superstructure with a ~25 Å periodicity (see inset in Figure 4.4.6). This structure is well-documented in the literature on thin iron oxide films grown on Pt(111) [79] and can unambiguously be assigned to an FeO(111) film, which consists of close-packed layers of iron and oxygen stacked as O-Fe-Pt(111). The Moiré superstructure originates from a mismatch between the Pt(111) and FeO(111) lattices. Since FeO(111) films can be grown on the Pt(100) surface as well [80], it seems plausible that the encapsulation by the FeO(111) layer also occurs on the side facets, which, according to the particles' habitus, expose (111) and (100) surfaces.

The mechanism of the encapsulation is still unknown. Nonetheless, the encapsulation implies high adhesion energy between Pt and iron oxide, which could, in principle, be derived from the structural information, obtained by STM on the particle size and shape, using the modified Wulff construction [81]. The analysis yielded an energy in the range of 3.8–4.2 J/m^2, which is, indeed, considerably larger than those obtained for Pd particles on $Fe_3O_4(111)$ and alumina films (i.e. 3.1–3.3 J/m^2), for which the encapsulation has not been observed [77]. Note also, that CO adsorption experiments indicated Fe-Pt surface intermixing with the onset at ca. 600 K [82], probably as the first step in the encapsulation.

The well-defined $Pt/Fe_3O_4(111)$ systems were examined in the CO oxidation reaction at near-atmospheric pressures and relatively low temperatures (~450 K) [84]. Figure 4.2.2A shows kinetic curves of CO_2 production under O-rich conditions (e.g. 10 mbar CO + 50 mbar O_2, He balance to 1 bar) over two samples possessing the same amount of Pt, but annealed either at 600 K (i.e. exposing clean Pt surface) or 850 K (i.e. encapsulated by FeO) prior to the reaction. The results for pristine

$Fe_3O_4(111)$ films and clean Pt(111) under the same conditions are also shown, for comparison.

It is clear that the encapsulated Pt particles exhibit higher reactivity than the clean Pt particles. The difference must be even higher if one normalizes the reactivity to the particles' surface area, which obviously decreases at 850 K due to particle sintering, albeit not measured in those experiments. The same effect was observed also at the stoichiometric ratio (40 mbar CO + 20 mbar O_2) [83]. Such promotional effect of encapsulation seems counterintuitive since the FeO film covering Pt particles and exposing a close-packed O layer must be essentially inert. In order to rationalize these findings on highly dispersed systems, we have to address the structure-reactivity relationships observed for extended, well-ordered FeO(111) films on Pt(111).

The FeO(111) film is, indeed, extremely stable and chemically inert under conditions typically used in UHV-based experiments. However, the situation changes dramatically in the mbar range of pressures. At low temperatures studied here (400–450 K), Pt(111) is inactive in CO oxidation due to the well-known blocking effect of CO on O_2 dissociation. The nanometer-thick $Fe_3O_4(111)$ films shows some activity, but it is negligible as compared to ultrathin FeO(111) films, which showed an order of magnitude higher reaction rate under the same conditions (Figure 4.4.7A). Therefore, it is the thin FeO overlayer on Pt that is responsible for the enhanced reactivity of encapsulated Pt particles in CO oxidation.

The experimental results in combination with DFT calculations provided compelling evidence that at elevated pressures the FeO(111) film transforms into a different structure containing an Fe layer sandwiched between two oxygen layers like O-Fe-O film (Figure 4.4.7B) [11, 12]. The mechanism for this transformation starts by O_2 adsorption on an Fe atom pulled out of the pristine FeO film. Because of local lowering of the work function by this process, electrons are transferred from the oxide/metal interface to oxygen, resulting in a transient superoxo species, which dissociates, thus forming the O-Fe-O structure. It appears, however, that the formation of the trilayer structure depends on the registry to underlying Pt(111), ultimately resulting in close-packed islands with a FeO_2 stoichiometry (see Figure 4.4.7B) rather than a continuous O-Fe-O film. Nonetheless, the topmost O atoms in the resulting FeO_{2-x} films are more weakly bound than those in the original FeO layer and readily react with incoming CO to form CO_2, which desorbs and leaves an oxygen vacancy behind. The overall activation barrier for CO_2 formation on the ideal O-Fe-O overlayer, as determined by DFT (~0.3 eV), is considerably lower than the computed barrier (~1 eV) for the CO oxidation reaction on Pt(111) and as such may explain higher reactivity of FeO(111)/Pt(111) than pure Pt(111) [12]. Certainly, to end the catalytic cycle, the oxygen vacancies must be replenished via the reaction with O_2 from the gas phase. Recent STM studies provided strong evidence for this mechanism of the Mars-van Krevelen type [84]. Interestingly, NO transforms the FeO film into the trilayer film in the same way as O_2. Comparison of the CO + O_2 and CO + NO reactions over the FeO(111)/Pt(111) surface showed that the replenishment of oxygen vacancies is the rate-limiting step that proceeds much faster with O_2 than NO [85].

It is important to note that both the transformation of the FeO into FeO_2-like film and the oxygen vacancy replenishment under the reaction conditions involve the
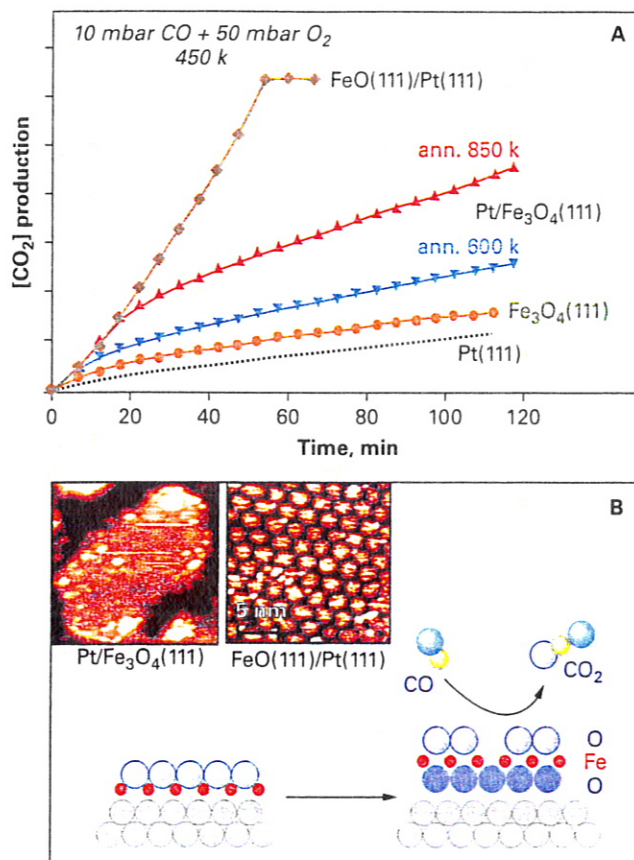
Figure 4.4.7 (A) CO_2 production over Pt(111), iron oxide films on Pt(111), and Pt/Fe_3O_4(111) annealed to 600 and 850 K. (B) STM images of the encapsulated Pt particle on Fe_3O_4(111) and, for comparison, of the FeO(111)/Pt(111) film, both exposed to 20 mbar O_2 at 450 K. The scheme illustrates the reaction mechanism. (See the text.)

charge transfer accompanied by a lattice distortion. Both factors favor the reaction on ultrathin films.

Apparently, the same scenario holds true for the encapsulated Pt particles. Figure 4.4.7B shows STM images of the encapsulated Pt particle on Fe_3O_4(111) and, for comparison, of the FeO(111)/Pt(111) film, both exposed to 20 mbar O_2 at 450 K. The close similarities between these two systems with respect to the surface morphology and reactivity indicate the absence of the "material gap," suggesting that the results and conclusions drawn for extended surfaces can be transferred to the supported nanoparticles.

In the experiments, presented in Figure 4.4.7A, the initial reaction rate over the encapsulated particles is almost identical to that measured on the FeO(111) film because the particle surface area (including both top and side facets) at the high Pt

loadings studied here is close to the surface area of the FeO film. Whereas the rate over the FeO film is almost constant until all CO in the ambient is consumed and the reaction stops, the reaction slows down over the encapsulated particles indicating catalyst deactivation. The latter may include carbon deposition, but this issue is beyond the scope of the present chapter.

This example demonstrates that ultrathin oxide films may enhance reactivity of metal catalysts, particularly in oxidation reactions in the low-temperature regime, where pure metal catalysts may suffer from site-blocking effects and strong chemisorption of reactants. A continuously growing body of studies on reactivity of ultrathin oxide films leads us to believe in a rational design of monolayer oxidation catalysts by combining different ultrathin films oxides with different metals, thereby controlling the charge transfer.

4.4.5 Fourth Case Study: Photochemistry at Nanoparticles

The coupling of molecules to surfaces strongly affects not only their thermal reaction paths but also the reactions between their excited states, which are accessible selectively by irradiation with photons (also primary or secondary electrons and other excitations can be used). This surface photochemistry has been investigated in detail for model systems comprising single-crystal surfaces and mostly rather simple adsorbate systems [86, 87]. Concentrating on the breaking of the surface bond or/and internal bonds, desorbing particles have often been used for characterization. Also, the changing coverages have been followed and characterized by some spectroscopy, which makes the observation of other induced changes accessible as well. The relevant differences to comparable gas-phase reactions have often been discussed under the heading "Desorption induced by electronic transitions (DIET)." These investigations have shown that the interaction with a surface can strongly change the absolute and relative probabilities of possible reaction paths [88]. The bases for these effects are the changes induced in excited-state potential energy surfaces by interaction with the surface, and in particular the possible exchange of charge and energy with the substrate during the excitation lifetime. On metals and semiconductors, this often leads to strong, selective quenching of the excited adsorbate states, which, because of its sensitive dependence on a number of adsorbate properties, can select certain pathways and suppress others. But also new channels can open up; in the range of low excitation energies (visible to near ultraviolet light), such channels often consist of transient negative ion (TNI) states [87].

It is a very interesting question which additional modifications are introduced if one uses nanoparticles instead of surfaces of bulk materials. As our earlier review [13] has summarized, for MNPs new electronic excitations – notably the Mie or particle Plasmon [20] – can be expected to feed photochemical reactions on the MNPs. But also the lifetimes and thus the reactivity of excited states may be changed by going to nanoparticles; the main expected effect here is the confinement of excitations in the small particles, which would quickly disperse in the volume in bulk materials [13].

In the past 7 years, we have examined this range of questions for an apparently simple (though in fact quite complex) system. Since one of the focal points was the influence of Mie plasmons, the chosen material was silver. The deposition of Ag NPs on ultrathin alumina films (on AlNi alloy surfaces) has been studied, and their properties have been characterized in detail [89]. The preparation of narrowly defined particle sizes in the range of 2–10 nm is possible. These particles possess a strong plasmonic mode at ~3.5 eV (polarized perpendicular to the surface; the lower energy parallel mode is screened by the close metal substrate), which has been observed and characterized by photon STM [89] (see Figure 4.4.8A) and by two-photon photoemission [90]. The thin alumina film decouples the Ag NPs quite efficiently electronically from the metal substrate without leading to charge-up, so that confinement effects might be expected. This is in contrast to the situation of Ag NPs on strongly reduced TiO_2 surfaces, where plasmon excitation leads to electron-hole pairs in the TiO_2 which decay radiatively [91]. NO was chosen as adsorbate because of the ease of its state-selective detection. Its adsorption on silver surfaces is, however, more complex than usually observed on (transition) metal surfaces. Because of its weak interaction with the noble metal silver, the adsorption has to be done below 80 K; in this range, NO dimers are formed on the surface. On Ag(111), the resulting adsorption layers have been characterized in great detail [92], including their photochemistry [93, 94], so that we were able to start on a good basis. The formation of dimers makes the photochemical reaction channels more complex: besides breaking of the ON-NO bond and the bond to the surface simultaneously, which leads to NO desorption into the gas phase (and some NO left on the surface), the dimers can also react to N_2O + O, which stays on the surface (N_2O can be detected by subsequent thermal desorption; adsorbed O leads to a stronger bond of the NO monomer, which desorbs thermally at a much higher temperature and has a much smaller photoreaction cross section than the dimer). Even the desorption of (extremely fast) N_2 molecules has been observed under certain conditions [95]. However, NO desorption is the strongest channel; it has been investigated in great detail. Besides measuring yields and desorption cross sections, the energy distributions over the translational [14] and internal modes (rotation, vibration) [96] of the desorbing NO have been measured. The influences of photon energy and polarization, particle size, and laser pulse duration have been investigated. In all cases, direct comparison to Ag(111) in the same experimental system and with the same methods has been made.

In the following, some of the main results are listed:

1. We found that the cross section, σ, for NO desorption from $(NO)_2$ monolayers on Ag NPs is indeed strongly enhanced by excitation of the plasmon, which is known to lie at approximately 3.5 eV (with a weak dependence on NP size [89, 90]). Compared to Ag(111), an enhancement of σ by up to a factor 40 (depending on NP size; see item 3 in this list) has been found [14].

2. There is also an enhancement of σ off the plasmon resonance, albeit weaker, which we interpret as due to confinement of excitations, here of hot electrons in the Ag NP. The photochemical mechanism of all the processes seen is believed to involve TNI states [87, 94], which is consistent with detailed characterizations
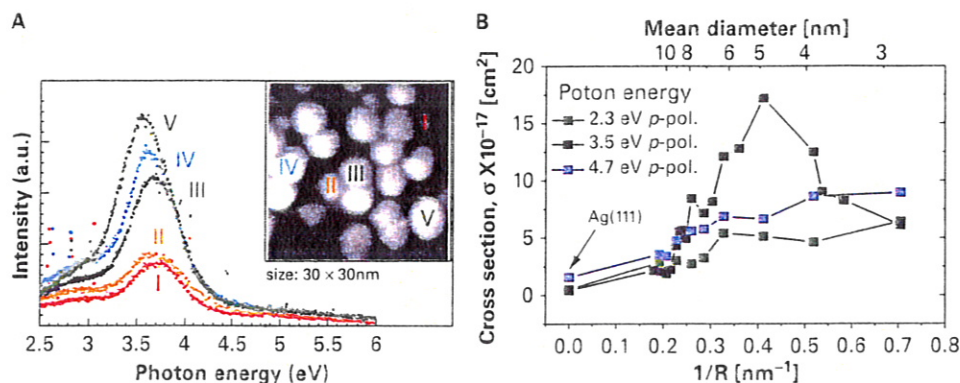
Figure 4.4.8 (A) Radiation emitted from individual Ag NPs of various sizes, observed with the photon STM. Inset: STM micrograph of the NP ensemble investigated. After [90]. (B) Variation of desorption cross sections, σ, of NO from $(NO)_2$ monolayers on Ag NPs as a function of mean particle size (top abscissa), for the three photon energies given. The plasmon is excited at 3.5 eV. The bottom abscissa gives the inverse radius and emphasizes the approximate scaling off the plasmon resonance. After [14].

of the desorbing NO ([96]; see item 4 in this list). This means that a hot electron of sufficient energy which is excited in an NP by the absorbed light tunnels from the NP into an adsorbed $(NO)_2$; in the formed TNI, the N-N and N-O bonds are weakened, and the bond to the surface is strengthened by the charge-image charge interaction, so that the corresponding wave packet is put into areas with potential gradients in all dimensions. When the electron jumps back into the NP after a very short residence time, a considerable fraction of the molecules has evolved sufficiently along the gradients to lead to breaking of the N-N and the NO-Ag bonds and to translational, rotational, and vibrational excitation of the NO that appears in the gas phase.

3. This cross-section enhancement is also size dependent (Figure 4.4.8B, [14]). It generally increases with decreasing NP size (diameter d), which we ascribe to confinement of the primary hot electrons in the NP ($\sigma \sim 1/d$, going with the surface/volume ratio S/V; see item 2 in this list). For excitation in the plasmon resonance, a strong maximum of σ at a certain NP size (here at $d \sim 5$ nm) is found, which is explained by two counteracting influences: on the one hand, the conversion of plasmons into hot electrons increases with decreasing NP size against the competing radiative decay; on the other hand, the total number of photons collected decays with the number of atoms in the particle [14, 96].

4. On the other hand, the dynamics of the bond dissociations (i.e. the motion of the representative wave packet on the potential energy surfaces of ground and excited states for the various molecular entities) turns out to be always the same. This is concluded from the fact that the final state of the desorbing NO stays constant: all energy distributions, translational, rotational, and vibrational, as well as their correlations, are identical despite the strong variations of cross sections [14, 96]. These characteristics are compatible with the proposed TNI mechanism (see item 2 in

this list). The only exception to this constancy of mechanism is found for excitation with the highest photon energy used (4.7 eV) and the smallest NPs ($d < 4$ nm). For these conditions, the mean translational energy of NO was considerably enhanced – in fact, a new, much faster component was found in addition to the normal one [14, 96]. We have explained this new path by excitation of a transient positive ion of the NO dimer that becomes accessible at an excitation energy sufficient to produce holes in the Ag d-band or direct excitations from a filled adsorbate state to empty states of the NP. That this path becomes observable only for very small NPs is due to the fact that its contribution is proportional to the surface area, while the TNI contribution goes down with the volume [14, 96].

5. All these experiments have been carried out with nanosecond lasers under fluences that lead to linear behavior of the photochemical yield with fluence (i.e. the determined cross sections are independent of fluence). This means that the excitations do not interact, even when they are confined in the NP. Very different behavior is found with femtosecond (~ 100 fs) lasers of even smaller fluences, for which the photons of a pulse arrive in a much shorter time so that the spatiotemporal photon density is increased by at least a factor of 10^4 [15]. Here the cross section is considerably enhanced and increases with fluence (i.e. the yield has nonlinear dependence on the fluence). With two-pulse measurements, in which one pulse is split into two and the two are delayed with respect to each other, it is found that the memory of the system is confined to the time of overlapping pulses. So there is a very short-lived confinement of interacting hot electrons. We have explained this by a repumping of hot electrons within the same pulse [15]. However, despite this dramatic change of reactivity, it is found again that the mechanism of desorption, as indicated by NO final state energies, is unchanged.

To summarize, we find that nanoparticles induce strong increases of photochemical cross sections if they possess strong new excitations, in particular of plasmon type. Also, confinement of excitations leads to (more gradual) enhancement of cross sections. If this confinement is also temporally constrained additional, nonlinear effects can be caused. The timescales of the electronic processes (including excitation and decay of plasmons) are very short, probably in the range below 10 fs (our results can only impose an upper limit of 100 fs). The dynamics of evolving molecular states, however, and thus the mechanism, appear essentially unchanged. This makes sense since these processes occur on much longer timescales. It cannot be excluded that there are systems in which the timescales can mix and, for example, the plasmon excitation has a direct photochemical influence; in fact, we have seen one such case [97], but we consider this as a probably rare, somewhat exotic case. While these results have been obtained with a particular system, we believe that these main conclusions will be fairly general, since they do not depend on any particular system properties.

As to the messages that might be carried over to practical photochemical processes, the main emphasis of the use of NPs should lie on the improved light harvesting made possible by plasmon excitations. The fact that plasmon resonances are fairly narrow, even if variations with particle size are utilized by using broadly varying ensembles, limits the usable part that can be caught of a broadband source like sun light. If one aims at photochemical reactions that require a certain energy, it will

be important to use NPs with plasmons in the required energy range. The additional effects offered by confinement will depend more strongly on the particular system since it is strongly influenced by the photochemical mechanism, which will not always be describable by the TNI process. Generally, we do not expect that particular new mechanisms will open up on NPs. The subject of photochemistry at nanoparticles is still in its infancy and deserves to be investigated more fully on a broader front, both for model systems and practical setups.

4.4.6 Synopsis

Via four case studies, this chapter has demonstrated how model studies on complex materials related to heterogeneous catalysis may help to unravel an atomistic view of processes at solid-vacuum, solid-gas, and solid-liquid interfaces. Going beyond metal single-crystal surfaces toward modeling some of the real complexity of catalytic materials is an important step forward to help designing energy-efficient catalysts by providing information on principles more than on specific systems. We are approaching a situation where the interplay between work on real catalytic material and work on specifically designed catalyst models may lead to a detailed understanding of the relation between structure-morphology and catalytic activity and selectivity.

4.4.7 References

1. Renn J, Schlögl R, Zenner H-P. Herausforderung Energie. Berlin: Max Planck Research Library for the History and Development of Knowledge, Proceedings 1; 2011.
2. Behrens M, Schlögl R. Energie ist Chemie – Katalyse als Schlüsseltechnik. Energie von Morgen: Eine Momentaufnahme. In: Renn J, Schlögl R, Zenner H-P, editors. Herausforderung Energie. Berlin: Max Planck Research Library for the History and Development of Knowledge, Proceedings 1); 2011. p. 163–74.
3. Freund H-J. Model studies in heterogeneous catalysis. Chem Eur J. 2010;16:9384–97.
4. Shaikhutdinov, S, and Freund, H-J. Ultrathin oxide Films on metal supports: structure-reactivity relations. Ann Rev Phys Chem. 2012;63:619–33.
5. Freund H-J, Pacchioni G. Oxide ultra-thin films on metals: new materials for the design of supported metal catalysts. Chem Soc Rev. 2008;37:2224–42.
6. Freund H-J. Clusters and islands on oxides: from catalysis via electronics and magnetism to optics. Surf Sci. 2002;500:271–99.
7. Duke CB. Surface science: the first thirty years. Surf Sci. 1994;299/300:vii–viii.
8. Freund H-J, Goodman DW. Ultrathin oxide films. In: Ertl G, Knözinger H, Schüth F, Weitkamp J, editors. Handbook of Heterogeneous Catalysis. Weinheim: Wiley-VCH Verlagsgesellschaft GmbH; 2008. p. 1309–38.
9. Shao X, Prada S, Giordano L, Pacchioni G, Nilius N, Freund H-J. Tailoring the shape of metal ad-particles by doping the oxide support. Angew Chem Int Ed. 2011;50:11525–7.
10. Wang H, Ariga H, Dowler R, Sterrer M, Freund H-J. Surface science approach to supported metal catalyst preparation – Pd deposition onto thin $Fe_3O_4(111)$ films from $PdCl_2$ precursor. J Catal. 2012;286:1–5.
11. Sun YN, Qin ZH, Lewandowski M, et al. Monolayer iron oxide film on platinum promotes low temperature CO oxidation. J Catal. 2009;266:359–68.

12. Sun YN, Giordano L, Goniakowski J, et al. The interplay between structure and CO oxidation catalysis on metal-supported ultrathin oxide films. Angew Chem Int Ed. 2010;49:4418–21.

13. Watanabe K, Menzel D, Nilius N, Freund H-J. Photochemistry on metal nanoparticles. Chem Rev. 2006;106:4301–20.

14. Mulugeta D, Kim KH, Watanabe K, Menzel D, Freund H-J. Size effects in thermal and photochemistry of $(NO)_2$ on Ag nanoparticles. Phys Rev Lett. 2008;101:146103-1-4.

15. Kim KH, Watanabe K, Mulugeta D, Freund H-J, Menzel D. Enhanced photoinduced desorption from metal nanoparticles by photoexcitation of confined hot electrons using femtosecond laser pulses. Phys Rev Lett. 2011;107:047401.

16. Molina LM, Hammer B. Some recent theoretical advances in the understanding of the catalytic activity of Au. Appl Catal A. 2005;291:21–31.

17. Green IX, Tang WJ, Neurock M, Yates JT. Spectroscopic observation of dual catalytic sites during oxidation of CO on a Au/TiO2 catalyst. Science. 2011;333:736–9.

18. Abbet S, Riedo E, Brune H, et al. Identification of defect sites on MgO(100) thin films by decoration with Pd atoms and studying CO adsorption properties. J Am Chem Soc. 2001;123:6172–8.

19. Ekardt W. Metal clusters. Chichester: John Wiley; 1999.

20. Kreibig U, Vollmer W. Optical properties of metal clusters. Berlin: Springer-Verlag; 1995.

21. Risse T, Shaikhutdinov S, Nilius N, Sterrer M, Freund H-J. Gold supported on thin oxide films: from single atoms to nanoparticles. Acc Chem Res. 2008;41:949–56.

22. Hashmi ASK, Hutchings GJ. Gold catalysis. Angew Chem Int Ed. 2006;45:7896–936.

23. Herzing AA, Kiely CJ, Carley AF, Landon P, Hutchings GJ. Identification of active gold nanoclusters on iron oxide supports for CO oxidation. Science. 2008;321:1331–5.

24. Valden M, Lai X, Goodman DW. Onset of catalytic activity of gold clusters on titania with the appearance of nonmetallic properties. Science. 1998;281:1647–50.

25. Chen MS, Goodman DW. The structure of catalytically active Au on titania. Science. 2004;306:252–5.

26. Mostafa S, Behafarid F, Croy JR, et al. Shape-dependent catalytic properties of Pt nanoparticles. J Am Chem Soc. 2010;132:15714–9.

27. Benedetti S, Myrach P, di Bona A, Valeri S, Nilius N, Freund H-J. Growth and morphology of metal particles on MgO/Mo(001): a comparative STM and diffraction study. Phys Rev B. 2011;83:125423 (1–10).

28. Benia HM, Nilius N, Freund HJ. Effect of electromagnetic interactions on plasmon excitations in silver particle ensembles. Surf Sci. 2006;600:128–33.

29. Brown M, Fujimori Y, Ringleb F, et al. Oxidation of Au by surface OH-nucleation and electronic structure of gold on hydrohylated MgO(001). J Am Chem Soc. 2011;133:10668–10676.

30. Goniakowski J, Noguera C. Electronic states and Schottky barrier height at metal/MgO (100) interfaces. Interface Sci. 2004;12:93–103.

31. Goniakowski J, Noguera C. Polarity of oxide surfaces and nanostructures. Rep Prog Phys. 2008;71:016501 (1–55).

32. Koplitz LV, Dulub O, Diebold U. STM study of copper growth on ZnO(0001)–Zn and ZnO(0001⁻)–O surfaces. J Phys Chem B. 2003;107:10583–90.

33. Pacchioni G, Giordano L, Baistrocchi M. Charging of metal atoms on ultrathin MgO/Mo (100) films. Phys Rev Lett. 2005;94:226104 (1–4).

34. Sterrer M, Risse T, Heyde M, Rust H-P, Freund H-J. Crossover from three-dimensional to two-dimensional geometries of Au nanostructures on thin MgO(001) films: a confirmation of theoretical predictions. Phys Rev Lett. 2007;98:206103-4.

35. Ricci D, Bongiorno A, Pacchioni G, Landman U. Bonding trends and dimensionality crossover of gold nanoclusters on metal-supported MgO thin films. Phys Rev Lett. 2006; 97:036106.

36. Nilius N, Ganduglia-Pirovano MV, Brázdová V, Kulawik M, Sauer J, Freund HJ. Counting electrons transferred through a thin alumina film into Au chains. Phys Rev Lett. 2008;100:096802.

37. Lin X, Nilius N, Freund HJ, et al. Quantum well states in two-dimensional gold clusters on MgO thin films. Phys Rev Lett. 2009;102:206801 (1–4).

38. Lin X, Nilius N, Sterrer M, Koskinen P, Haekkinen H, Freund H-J. Characterizing low-coordinated atoms at the periphery of MgO-supported Au islands using scanning tunneling microscopy and electronic structure calculations. Phys Rev B. 2010;81:153406 (1–4).

39. Lin X, Yang B, Benia HM, et al. Charge-mediated adsorption behavior of CO on MgO-supported Au clusters. J Am Chem Soc. 2010;132:7745–9.

40. Frondelius P, Häkkinen H, Honkala K. Formation of gold(I) edge oxide at flat gold nanoclusters on an ultrathin MgO film under ambient conditions. Angew Chem Int Ed. 2010;49:7913–6.

41. Gianfranco P. Ab initio theory of point defects in oxide materials: structure, properties, chemical reactivity. Solid State Sci. 2000;2:161–79.

42. McKenna KP, Shluger A. Electron-trapping polycrystalline materials with negative electron affinity. Nat Mater. 2008;7:859–62.

43. Benia HM, Myrach P, Gonchar A, Risse T, Nilius M, Freund HJ. Electron trapping in misfit dislocations of MgO thin films. Phys Rev B. 2010;81:241415.

44. Sterrer M, Yulikov M, Fischbach E, et al. Interaction of gold clusters with color centers on MgO(001) films. Angew Chem Int Ed. 2006;45:2630–2.

45. Wang JX, Lunsford JH. Characterization of [Li+O] centers in lithium-doped magnesium oxide catalysts. J Phys Chem. 1986;90:5883–7.

46. Ito T, Wang J, Lin CH, Lunsford JH. Oxidative dimerization of methane over a lithium-promoted magnesium oxide catalyst. J Am Chem Soc. 1985;107:5062–8.

47. Rodriguez JA, Hanson JC, Kim J-Y, Liu G, Iglesias-Juez A, Fernández-García M. Properties of CeO_2 and $Ce_{1-x}Zr_xO_2$ nanoparticles: X-ray absorption near-edge spectroscopy, density functional, and time-resolved X-ray diffraction studies. J Phys Chem B. 2003; 107:3535–43.

48. Nambu A, Graciani J, Rodriguez JA, Wu Q, Fujita E, Sanz JF. N doping of $TiO_2(110)$: photoemission and density-functional studies. J Chem Phys. 2006;125: 094706.

49. Pala RGS, Metiu H. The structure and energy of oxygen vacancy formation in clean and doped, very thin films of ZnO. J Phys Chem C. 2007;111:12715–22.

50. Nolan M, Verdugo VS, Metiu H. Vacancy formation and CO adsorption on gold-doped ceria surfaces. Surf Sci. 2008;602:2734–42.

51. Shao X, Nilius N, Freund H-J. Li/Mo co-doping of CaO films: a means to tailor the equilibrium shape of Au deposits. J Am Chem Soc. 2012;134:2532–2534.

52. Stavale F, Nilius N, Freund H-J. Cathodoluminescence spectroscopy of near-surface centres in Cr doped MgO(001) thin films by scanning tunnelling microscopy. New J Phys. 2012;14:033006-1-14.

53. Henderson B, Imbusch GF. Optical spectroscopy of inorganic solids. Oxford: Oxford University Press; 1989.

54. Hu Z, Li B, Sun X, Metiu H. Chemistry of doped oxides: the activation of surface oxygen and the chemical compensation effect. J Phys Chem C. 2011;115:3065–74.

55. Myrach P, Nilius N, Levchenko S, et al. Temperature-dependent morphology, magnetic and optical properties of Li-doped MgO. ChemCatChem. 2010;2:854–62.

56. Campbell CT. Ultrathin metal films and particles on oxide surfaces: structural, electronic and chemisorptive properties. Surf Sci Rep. 1997;27:1–111.

57. Fu Q, Wagner T. Interaction of nanostructured metal overlayers with oxide surfaces. Surf Sci Rep. 2007;62:431–98.

58. Ertl G, Knözinger H, Schüth F, Weitkamp J. Handbook of heterogeneous catalysis. Weinheim: Wiley-VCH; 2008.

59. de Jong KP. Synthesis of solid catalysts. Weinheim: Wiley-VCH; 2009.

60. Regalbuto JR, Navada A, Shadid S, Bricker ML, Chen Q. An experimental verification of the physical nature of Pt adsorption onto alumina. J Catal. 1999;184:335–48.

61. Weiss W, Ritter M. Metal oxide heteroepitaxy: Stranski-Krastanov growth of iron oxides on Pt(111). Phys Rev B. 1999;59:5201–13.

62. Hao X, Spieker WA, Regalbuto JR. A further simplification of the revised physical adsorption (RPA) model. J Colloid Interface Sci. 2003;267:259–64.

63. Olsbye U, Wendelbo R, Akporiaye D. Stucy of Pt/alumina catalyst preparation. Appl Catal A. 1997;152:127–41.

64. Spieker WA, Regalbuto JR. A fundamental model of platinum impregnation onto alumina. Chem Eng Sci. 2001;56:3491–504.

65. Bozon-Verduraz F, Omar A, Escard J, Pontvianne B. Chemical state and reactivity of supported palladium: I. characterization by XPS and UV-visible spectroscopy. J Catal. 1978;53:126–134.

66. Fleisch TH, Hicks RF, Bell AT. An XPS study of metal-support interactions on $PdSiO_2$ and $PdLa_2O_3$. J Catal. 1984;87:398.

67. Wang, H-F, Kaden, WE, Dowler, R, Sterrer, M, and Freund, H-J. Model oxide-supported metal catalysts – comparison of ultrahigh vacuum and solution based preparation of Pd nanoparticles on a single-crystalline oxide substrate. Phys Chem Chem Phys. 2012;14:11525–11533.

68. Tauster SJ. Strong metal-support interactions. Acc Chem Res. 1987;20:389–94.

69. Tauster SJ, Fung SC, Garten RL. Strong metal-support interactions. Group 8 noble metals supported on titanium dioxide. J Am Chem Soc. 1978;100:170–5.

70. Ko EI, Garten RL. Ethane hydrogenolysis studies of TiO_2-supported group VIII metal catalysts. J Catal. 1981;68:233–6.

71. Haller GL, Resasco DE. Metal-support interactions between Group VIII metals and reducible oxides. Adv Catal. 1989;36:173.

72. Bernal S, Calvino JJ, Cauqui MA, et al. Some recent results on metal/support interaction effects in NM/CeO_2 (NM: noble metal) catalysts. Catal Today. 1999;50:175–206.

73. Dulub O, Hebenstreit W, Diebold U. Imaging cluster surfaces with atomic resolution: the strong metal-support interaction state of Pt supported on TiO_2(110). Phys Rev Lett. 2000;84:3646.

74. Bowker M, Stone P, Morrall P, et al. Model catalyst studies of the strong metal–support interaction: surface structure identified by STM on Pd nanoparticles on TiO_2(110). J Catal. 2005;234:172–81.

75. Barcaro G, Agnoli S, Sedona F, Rizzi GA, Fortunelli A, Granozzi G. Structure of reduced ultrathin TiOx polar films on Pt(111). J Phys Chem C. 2009;113:5721–9.

76. Netzer FP, Allegretti F, Surnev S. Low-dimensional oxide nanostructures on metals: hybrid systems with novel properties. J Vac Sci Technol B. 2010;28:1–16.

77. Qin ZH, Lewandowski M, Sun YN, Shaikhutdinov S, Freund HJ. Encapsulation of Pt nanoparticles as a result of strong metal-support interaction with Fe_3O_4(111). J Phys Chem C. 2008;112:10209–13.

78. Qin ZH, Lewandowski M, Sun YN, Shaikhutdinov S, Freund HJ. Morphology and CO adsorption on platinum supported on thin Fe_3O_4(111) films. J Phys Condens Matter. 2009;21:134019.

79. Weiss W, Ranke W. Surface chemistry and catalysis on well-defined epitaxial iron-oxide layers. Prog Surf Sci. 2002;70:1–151.
80. Shaikhutdinov S, Ritter M, Weiss W. Hexagonal heterolayers on a square lattice: a combined STM and LEED study of FeO(111) on Pt(100). Phys Rev B. 2000;62:7535–41.
81. Hansen KH, Worren T, Stempel S, et al. Palladium nanocrystals on Al_2O_3: structure and adhesion energy. Phys Rev Lett. 1999;83:4120–3.
82. Sun YN, Qin ZH, Lewandowski M, Shaikhutdinov S, Freund HJ. CO adsorption and dissociation on iron oxide supported Pt particles. Surf Sci. 2009;603:3099–103.
83. Lewandowski M, Sun YN, Qin ZH, Shaikhutdinov S, Freund HJ. Promotional effect of metal encapsulation on reactivity of iron oxide supported Pt catalysts. Appl Catal A. 2011;391:407–10.
84. Lewandowski M, Groot IMN, Shaikhutdinov S, Freund HJ. Scanning tunneling microscopy evidence for the Mars-van Krevelen type mechanism of low temperature CO oxidation on an FeO(111) film on Pt(111). Catal. Today. 2012;181:52–55.
85. Lei Y, Lewandowski M, Sun Y-N, et al. CO+NO versus CO+O_2 reaction on monolayer FeO(111) films on Pt(111). ChemCatChem. 2011;3:671–4.
86. Dai H-L, Ho W. Laser spectroscopy and photochemistry on metal surfaces. Singapore: World Scientific; 1995.
87. Zimmermann FM, Ho W. State resolved studies of photochemical dynamics at surfaces. Surf Sci Rep. 1995;22:127–247.
88. Menzel D. Electronically induced surface chemistry: localised bond breaking versus delocalisation. Surf Interface Anal. 2006;38:1702–11.
89. Nilius N, Ernst N, Freund HJ. Photon emission spectroscopy of individual oxide-supported silver clusters in a scanning tunneling microscope. Phys Rev Lett. 2000;84:3994–7.
90. Evers F, Rakete C, Watanabe K, Menzel D, Freund H-J. Two-photon photoemission from silver nanoparticles on thin alumina films: role of plasmon excitation. Surf Sci. 2005;593:43–8.
91. Nilius N, Ernst N, Freund H-J. On energy transfer processes at cluster-oxide interfaces: silver on titania. Chem Phys Lett. 2001;349:351–7.
92. Carlisle CI, King DA. Direct molecular imaging of NO monomers and dimers and a surface reaction on Ag(111). J Phys Chem B. 2001;105:3886–93.
93. Vondrak T, Burke DJ, Meech SR. The dynamics and origin of NO photodesorbed from NO/Ag(111). Chem Phys Lett. 2000;327:137–42.
94. So SK, Franchy R, Ho W. Photodesorption of NO from Ag(111) and Cu(111). J Chem Phys. 1991;95:1385–99.
95. Kim KH, Watanabe K, Menzel D, Freund H-J. Photoinduced abstraction reactions within NO dimers on Ag(111). J Am Chem Soc. 2009;131:1660–1.
96. Mulugeta D, Watanabe K, Menzel D, Freund H-J. State-resolved investigation of the photodesorption dynamics of NO from $(NO)_2$ on Ag nanoparticles of various sizes in comparison with Ag(111). J Chem Phys. 2011;134:164702 (1–11).
97. Watanabe K, Kim KH, Menzel D, Freund H-J. Hyperthermal chaotic photodesorption of xenon from alumina-supported silver nanoparticles: plasmonic coupling and plasmon-induced desorption. Phys Rev Lett. 2007;99:225501.